

## Article

# Dynamic Simulations on Enhanced Heat Recovery Using Heat Exchange PCM Fluid for Solar Collector

Yawen Ren and Hironao Ogura \* 

Graduate School of Science and Engineering, Chiba University, Chiba 263-8522, Japan; renyawen@chiba-u.jp

\* Correspondence: oguralab@outlook.jp or hiro\_ogura@faculty.chiba-u.jp

**Abstract:** Facing the goal of carbon neutrality, energy supply chains should be more low-carbon and flexible. A solar chemical heat pump (SCHP) is a potential system for achieving this goal. Our previous studies developed a silicone-oil-based phase-change material (PCM) mixture as a PCM fluid for enhancing heat recovery above 373 K in the solar collector (SC) of the SCHP. The PCM fluid was previously tested to confirm its dispersity and flow properties. The present study proposed a 3D computational fluid dynamics model to simulate the closed circulation loop between the SC and reactor using the PCM fluid. The recovered heat in the SC was studied using several flow rates, as well as the PCM weight fraction of the PCM fluid. Furthermore, the net transportable energy is considered to evaluate the ratio of recovered heat and relative circulation power. As a result, it was verified that the recovered heat of the SC in the experiment and simulation is consistent. The total recovered heat is improved using the PCM fluid. A lower flow rate can enhance the PCM melting mass and the recovered heat although sensible heat amount increases with the flow rate. The best flow rate was 1 L/min when the SC area is 1 m<sup>2</sup>. Furthermore, the higher PCM content has higher latent heat. On the other hand, the lower content PCM can increase the temperature difference between the SC inlet and outlet because of the lower PCM heat capacity. For the 1 L/min flow rate, 2 wt% PCM fluid has shorter heat-storing time and larger net transportable energy than 0 wt% PCM fluid (426 kJ←403 kJ) for the SCHP unit.

**Keywords:** solar thermal; computational fluid dynamics; latent heat; multiphase flow; transportable energy; chemical heat pump



**Citation:** Ren, Y.; Ogura, H. Dynamic Simulations on Enhanced Heat Recovery Using Heat Exchange PCM Fluid for Solar Collector. *Energies* **2023**, *16*, 3075. <https://doi.org/10.3390/en16073075>

Academic Editor: Frede Blaabjerg

Received: 28 February 2023

Revised: 24 March 2023

Accepted: 25 March 2023

Published: 28 March 2023



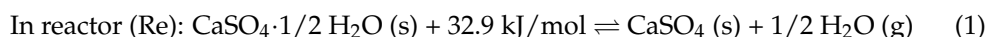
**Copyright:** © 2023 by the authors. Licensee MDPI, Basel, Switzerland. This article is an open access article distributed under the terms and conditions of the Creative Commons Attribution (CC BY) license (<https://creativecommons.org/licenses/by/4.0/>).

## 1. Introduction

The Japanese government [1] and the governments of many other countries around the world have made legal commitments to carbon neutrality by 2050; this has become a catalyst for expanding the introduction of regional renewable energy and recovering the waste energy existing in urban areas. Independent and decentralized energy systems utilizing local unutilized resources, such as solar energy, can support these movements.

A solar chemical heat pump (SCHP) is a potential stand-alone energy supply system for this goal. The SCHP unit is composed of the solar collector (SC) subunit, the connecting pipes (CPs) subunit, and the chemical heat pump (CHP) main unit. The SC subunit provides the solar heat source to the CHP main unit. The CHP main unit has been studied in our laboratory for many decades [2–8]. The CHP main unit is a closed system that is composed of a reactor (Re) and a condenser/evaporator (Co/Ev). As shown in Equations (1) and (2), the CHP main unit operates based on the reliable solid–gas thermochemical reversible reactions. In the heat-storing step, the SC subunit collects and transfers solar thermal to the Re via the CPs subunit. Then, solar heat can be stored as high-density chemical heat in the Re without heat loss based on the reversible endothermic reactions of Equation (1). In the heat-releasing step, the hot heat for heating and hot water supply is released in the Re based on the reversible exothermic reaction of Equation (1), meanwhile, the cold heat for cooling and refrigeration can be released in the evaporator according to Equation (2). The

CHP main unit can operate efficiently and does not release any toxic and greenhouse gases.



In the SCHP unit, the heat recovery efficiency of the heat transfer fluid (HTF) circulating in the SC and Re affects the performance of the overall system. Using phase-change material (PCM) is one of the methods to enhance the heat recovery efficiency. Many methods have been studied in this field. According to whether PCM has direct contact with HTF, it can be divided into indirect and direct contact systems.

Many studies of indirect contact systems have focused on alleviating the obstacles of the limited thermal conductivity of the PCM [9,10]. Such studies include those using fins and composite materials formed by various means. Studies using appropriate fins materials [11–13] and fins configuration [14–17] in shell-and-tube heat exchangers are proven and cost-effective solutions for enhancing the heat transfer of PCM [18,19]. Other studies use composite PCM formed by high thermal conductivity nanoparticles (e.g., copper [20], titanium dioxide [21], and aluminum oxide [22]) and found that PCM can effectively improve the heat transfer efficiency, and the stability of the composite PCMs can be increased by surfactant addition/modification [23–25], changing pH values [26], and adding oscillating movement [27]. Moreover, other studies use porous metal foam with good chemical stability and high stiffness and PCM forms another composite PCM that can also significantly enhance the solid/liquid phase transition heat transfer [28–30] and also ensure a more uniform phase transition process of the composites [31].

The direct contact between PCM and HTF has a simpler structure and higher energy density because there is no wall thermal resistance for heat transfer [32,33]. Increasing the residence time of HTF flowing in the PCM layer can improve the PCM charging performance [34], and the HTF flowing uniformly can make the PCM discharge the latent heat efficiently [35]. However, because of the different physical properties of HTF and PCM, when the HTF cannot flow uniformly or the PCM solidifies and causes deposition, the two substances are easily delaminated to increase the heat transfer path and even form a solid PCM dead zone or cause pipe blockage [32,36].

Adding latent heat transfer functions to HTF can be considered as a solution to increase the overall specific heat for enhancing recovered heat. Based on the operating principle of the SCHP unit, silicone oil serves as the base of the HTF, and erythritol was selected as a PCM due to its high latent heat and suitable melting point. Erythritol is mixed and dispersed into silicone oil as a mixed HTF that can be used at temperatures above 100 °C. Oleyl alcohol as the surfactant is added into the mixed HTF to improve dispersion stability. The silicone-oil-based PCM mixture is called PCM fluid in this study.

The PCM fluid has been examined in a previous study [37], which included observational experiments on the stability of PCM particle dispersion, as well as differential scanning calorimetry (DSC) and viscosity measurements. Additionally, single straight pipe preparatory experiments were conducted using the PCM fluid. The previous study demonstrated the following results. (1) After stirring at 700 rpm and heating until the erythritol was melted, the mixture did not agglomerate upon natural cooling because the oleyl alcohol, which has long hydrophobic groups, weakened the hydrophilicity of the erythritol interface. This inhibited the aggregation of erythritol particles and adhesion to glass surfaces. (2) According to the DSC curve of pure erythritol and that of the mixture of 10 wt% erythritol, 4 wt% oleyl alcohol, and 86 wt% silicone oil, the change in the melting point was not sensitive. (3) Oleyl alcohol has a lower viscosity than silicone oil, and there was no noticeable change in the viscosity of the mixture. Finally, (4) based on the single straight pipe preparatory experiments, the pressure drop of 10 wt% PCM fluid did not increase significantly.

In this study, we introduce the PCM fluid into the circulation of the SCHP unit. The previous study [38] found that it is difficult to simulate the HTF circulating in the SCHP using the finite differential method in Microsoft Excel. Hence, to investigate the melting process of the PCM in the SC and to determine the amount of recovered heat through latent and sensible heat, we have developed a dynamic simulation model using the finite volume method including the heat and mass transfer of the phase-changing process, which was solved in ANSYS Fluent 2021 R2 (21.2), a commercial software. We examine the effects of varying flow rates and PCM weight fraction on the melting mass and recovered heat using the model. Additionally, we consider the net transportable energy to identify effective strategies for heat recovery in the SC of the SCHP unit using the PCM fluid, and the trial estimation of heat storing time can prove that the usage of PCM fluid can enhance the performance of the SCHP unit.

## 2. Methodology

### 2.1. Descriptions of SCHP Unit

Figure 1 depicts the schematic diagram of the SCHP unit. The unit consists of four components. (1) The forced circulation evacuated solar collector (SC) containing a compound parabolic collector (CPC) reflector: this component recovers solar irradiation and uses it to heat the HTF. The SC is set at an inclination angle of  $30^\circ$  that is preferred in the summer season, and a pyranometer is set on the SC with the same tilt angle. (2) The reactor (Re): a key component where the recovered solar heat is used to drive the chemical reaction in the reactant bed to produce hot heat; detailed information on the Re has been described in our previous study [8]. (3) The connection pipes (CPs): these pipes connect the SC and the Re, allowing the heated HTF to transfer the recovered heat to the Re for use. (4) The condenser/evaporator (Co/Ev): the details of the Co/Ev are described in [39]. Overall, the SCHP unit appears to be a well-designed unit that utilizes solar heat in an efficient and effective way.

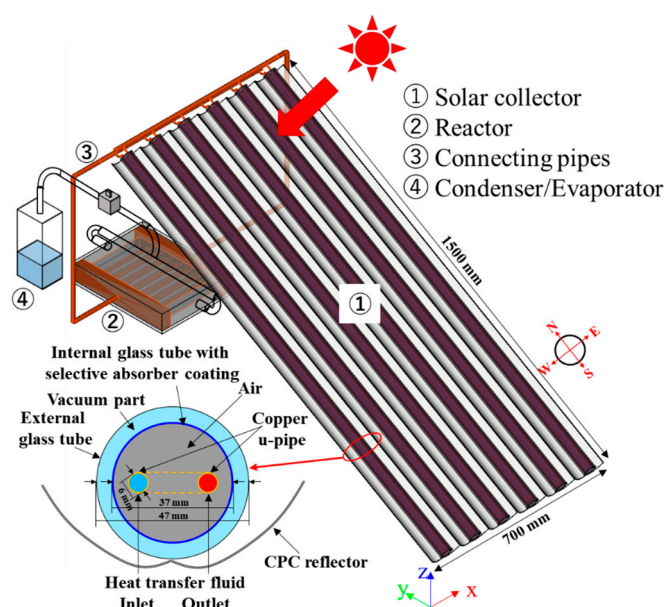


**Figure 1.** A schematic diagram of the SCHP unit.

### 2.2. Mathematical Model for Circulation Loop of HTF in the SCHP Unit

This study proposes a 3D computational fluid dynamics (CFD) model to simulate the closed circulation loop of the HTF based on the above SCHP unit size for heat recovery in the SC. The model is developed with the finite volume method (FVM) and solved in ANSYS Fluent 2021 R2. The model adopts the mixture model for multiphase flow simulation. The mixture model is a simplified scheme for the full Eulerian multiphase model, and it is

applicable for liquid–solid flows [40]. The heat and mass transfer in the phase transition process are realized through user-defined functions (UDFs). The flow of the PCM fluid in the pipes of the model is transient, turbulent, and incompressible. The specifications of the circulation loop in the SCHP unit are provided in Table 1, while Table 2 presents the thermophysical properties of the mixed PCM fluid.

**Table 1.** Specifications of the circulation loop in the model.

| Component                               | Properties/Unit                 | Value       |
|---|---------------------------------|-------------|
| Evacuated glass tubes<br>(Borosilicate) | Number                          | 6           |
|   | Outer/inner diameter (mm)       | 47.00/37.00 |
|   | Transmittance of outer glass    | 0.92        |
|   | Emissivity of outer glass       | 0.90        |
|   | Absorbance of selective coating | 0.94        |
|   | Emissivity of selective coating | 0.06        |
| Manifold u-pipes (copper)               | Inner diameter (mm)             | 6.00        |
|   | Length (mm)                     | 1500        |
| CPC reflector                           | Reflectance                     | 0.94        |
| Connecting pipes (SUS304)               | Inner diameter (mm)             | 14.60       |
|   | Total length (mm)               | 2495        |

**Table 2.** Thermophysical properties of the PCM fluid.

| Fluid                        | Properties/Unit   | Value  |
|------------------------------|---|--|
| Base of HTF (silicone oil)   | Density ( $\text{kg}/\text{m}^3$ )                          | $-0.93T + 1241$  |
|                              | Specific heat ( $\text{J}/(\text{kg}\cdot\text{K})$ )       | $1.4T + 1097$  |
|                              | Viscosity (Pas)   | $10^{10-0.84+\text{LOG}(T)+2.3} \times 10^{-6} \cdot \rho$ |
|                              | Thermal conductivity ( $\text{W}/(\text{m}\cdot\text{K})$ ) | 0.13   |
| Solid PCM (erythritol) [41]  | Density ( $\text{kg}/\text{m}^3$ )                          | 1480   |
|                              | Specific heat ( $\text{J}/(\text{kg}\cdot\text{K})$ )       | 1350   |
|                              | Viscosity (Pas)   | 0.02895  |
|                              | Thermal conductivity ( $\text{W}/(\text{m}\cdot\text{K})$ ) | 0.732  |
| Liquid PCM (erythritol) [41] | Density ( $\text{kg}/\text{m}^3$ )                          | 1300   |
|                              | Specific heat ( $\text{J}/(\text{kg}\cdot\text{K})$ )       | 2740   |
|                              | Viscosity (Pas)   | 0.01602  |
|                              | Thermal conductivity ( $\text{W}/(\text{m}\cdot\text{K})$ ) | 0.326  |
|                              | Latent heat ( $\text{kJ}/\text{kg}$ )                       | 340  |
|                              | Melting temperature (K)                                     | 390.15   |

### 2.2.1. Assumptions

To simplify the complex practical mathematical model and optimize the computational cost, the following scientific settings and assumptions are made:

1. The preparation processes of the PCM fluid are not considered in the simulation.
2. The solid erythritol at ambient temperature is distributed uniformly in silicone oil.
3. The received solar heat flux at different positions of the SC is uniform.
4. The solar irradiation absorbed by the outer glass tube is neglected.
5. The heat loss caused by the evacuated glass tube is neglected.
6. The thermal resistance caused by the thickness of the glass tube in SC is neglected.
7. The continuum surface force model [42] in ANSYS Fluent is used to represent that the surface tension at the PCM–silicone oil interface decreases when the surfactant is adsorbed on the PCM surface.

### 2.2.2. Initial and Boundary Conditions

Table 3 presents the initial conditions and boundary conditions in the model. As shown in Equation (3), the initial temperature of the domain is ambient temperature, the initial operation pressure is atmospheric pressure, and the initial velocity is zero. Equations (4) and (5) show that the certain thermal heat flux is provided to simulate the heat of the u-pipes from solar radiation. Furthermore, Equations (6)–(8) present that all external surfaces of the SChP system are set to a certain external heat loss coefficient. Equation (9) shows the pressure gradient normal to the boundary is time-dependent and depends on spatial coordinates, simulated in ANSYS Fluent. Equation (10) presents that the no-slip wall boundary condition is used for all boundaries involving viscous fluids and solid boundaries.

**Table 3.** Initial conditions and boundary conditions in the model.

| Type                 | Location            | Formula  |      |
|----------------------|---------------------|--|------|
| Initial Conditions:  |                     |  |      |
| Temperature          | All domains         | $t = 0 : T = T_{atm} = 298.15 \text{ K}$   | (3)  |
| Pressure             | All domains         | $t = 0 : P = P_{atm} = 101.325 \text{ kPa}$  |      |
| Velocity             | All domains         | $t = 0 : v = 0 \text{ m/s}$  |      |
| Boundary Conditions: |                     |  |      |
| Temperature          | The front of the SC | $\lambda \frac{\partial E}{\partial n} = c_p \cdot \tau_g \cdot \sigma \cdot I_r$                  | (4)  |
|                      | The back of the SC  | $\lambda \frac{\partial E}{\partial n} = \eta_{cpc} \cdot c_p \cdot \tau_g \cdot \sigma \cdot I_r$ | (5)  |
|                      | The CPs             | $\lambda \frac{\partial E}{\partial n} = h_{cp} \cdot c_p \cdot (T - T_{atm})$                     | (6)  |
|                      | The pipes in the Re | $\lambda \frac{\partial E}{\partial n} = h_{th} \cdot c_p \cdot (T - T_{atm})$                     | (7)  |
|                      | The frame in the Re | $\lambda \frac{\partial E}{\partial n} = h_f \cdot c_p \cdot (T - T_{atm})$                        | (8)  |
| Pressure             | All boundaries      | $\frac{\partial P}{\partial n} = G(t, x, y, z)$  | (9)  |
| Velocity             | All boundaries      | $v _{attheboundary} = v_{wall} = 0$  | (10) |

$I_r$ , global solar irradiation ( $W/m^2$ );  $\tau_g$ , transmittance of the outer glass;  $\sigma$ , absorbance of the selective coating;  $\eta_{cpc}$ , reflectance of the CPC reflector;  $n$ , the normal direction of the HTF surface.

### 2.2.3. Governing Equations

This subsection contains the governing equations involved in this model: continuity equation, momentum equation, energy equation, and mass transfer balance equations.

Continuity equation:

$$\frac{\partial \rho}{\partial t} + \nabla \cdot (\rho v) = 0 \tag{11}$$

Momentum equation:

$$\frac{\partial}{\partial t}(\rho v) + \nabla \cdot (\rho v v) = -\nabla p + \nabla \cdot (\mu (\nabla v + \nabla v^T)) + Z + \rho g + \nabla \cdot \left( \sum_{i=1}^n \alpha_i \rho_i (v_i - v)(v_i - v) \right) \tag{12}$$

Energy equation:

$$\frac{\partial}{\partial t}(\rho E) + \nabla \cdot (v(\rho E + p)) = \nabla \cdot (\lambda \nabla T) + S_{lat} \tag{13}$$

$$S_{lat} = \begin{cases} \Delta H_{lat} \dot{m}_{l \rightarrow s}, & T < T_m \\ -\Delta H_{lat} \dot{m}_{s \rightarrow l}, & T \geq T_m \end{cases} \tag{14}$$

$\rho$  is the mixture density calculated by the volume average of each phase, and  $v$  is the mass-averaged velocity of each phase.  $Z$  is the body force, referring to the force due to surface tension, and  $\mu$  is the volume-averaged viscosity of the multiphase flow.  $E$  is the summary of the sensible enthalpy for each phase,  $\lambda$  is the effective thermal conductivity, and  $S_{lat}$  shown in Equation (14) is the volumetric heat source of solid–liquid phase changes.  $\Delta H_{lat}$  is the latent heat, and  $T_m$  is the melting point of the PCM.  $\dot{m}_{l \rightarrow s}$  is the mass transfer

rate from the liquid to the solid phase and  $\dot{m}_{s \rightarrow l}$  is that from the solid to liquid phase; both can be described based on the temperature range [43]:

$$\begin{cases} \dot{m}_{s \rightarrow l} = \zeta \cdot \alpha_l \rho_l \frac{(T - T_m)}{T_m}, & T \geq T_m \\ \dot{m}_{l \rightarrow s} = \zeta \cdot \alpha_s \rho_s \frac{(T_m - T)}{T_m}, & T < T_m \end{cases} \quad (15)$$

Mass balance equations in phase changing:

$$\begin{cases} \frac{\partial}{\partial t}(\alpha_l \rho_l) + \nabla \cdot (\alpha_l \rho_l \mathbf{v}) = -\nabla \cdot (\alpha_l \rho_l (\mathbf{v}_l - \mathbf{v})) + (\dot{m}_{s \rightarrow l} - \dot{m}_{l \rightarrow s}) \\ \frac{\partial}{\partial t}(\alpha_s \rho_s) + \nabla \cdot (\alpha_s \rho_s \mathbf{v}) = -\nabla \cdot (\alpha_s \rho_s (\mathbf{v}_s - \mathbf{v})) + (\dot{m}_{l \rightarrow s} - \dot{m}_{s \rightarrow l}) \end{cases} \quad (16)$$

$\zeta$  is the coefficient that can be interpreted as a relaxation time, which is 0.3 in this study.  $\alpha$  is the volume fraction of the represented phase.

The above-governing equations' boundary conditions are solved with a pressure-based implicit algorithm. The viscous model uses the standard k-epsilon model. Pressure-velocity coupling is solved with a SIMPLE scheme. Spatial discretization of the gradient uses the least squares cell-based scheme. Pressure is PRESTO! scheme. Momentum, volume fraction, turbulent kinetic energy, turbulent kinetic energy, turbulent dissipation rate, and energy are discretized with a first-order upwind scheme. With regard to solution control, under-relaxation factors of pressure, density, body forces, momentum, slip velocity, volume fraction, turbulent kinetic energy, turbulent dissipation rate, turbulent viscosity, and energy are 0.3, 1.0, 1.0, 0.3, 0.1, 0.3, 0.3, 0.3, 1.0, and 1.0, respectively. Absolute criteria of residual for continuity, velocity, energy, k, epsilon, and volume fraction are  $10^{-3}$ ,  $10^{-3}$ ,  $10^{-6}$ ,  $10^{-3}$ ,  $10^{-3}$ , and  $10^{-3}$ .

#### 2.2.4. Net Transportable Energy

This study introduces the net transportable energy of total recovered heat minus the relative theoretical circulation power to evaluate the change of circulation power caused by the change of specific viscosity. The net transportable energy is calculated by Equation (17). The relative theoretical circulation power is calculated by Equation (18).

$$\xi = \text{Total recovered heat (kJ)} - \text{Relative theoretical circulation power (kJ)} \quad (17)$$

$$W_c = Q\Delta P = \rho Q \sum E_{in} = \rho Q (M_{loss,fr} + M_{loss,lo} + M_{loss,int}) \quad (18)$$

$W_c$  is the relative theoretical circulation power without considering the circulation pump efficiency.  $M_{loss,fr}$  is the piping friction energy loss (J/kg), calculated by Darcy-Weisbach Equation.  $M_{loss,lo}$  is the local pressure drop, which includes sudden expansions or contractions, bends, confluences, valves, and joints.  $M_{loss,int}$  is the internal loss of the circulating pump, which is an indispensable part in a closed circulation. The internal pump loss used in this study is 5.5 W.

### 3. Results and Discussions

In this section, we first verify the grid and time-step independence before proceeding with the simulations. We compare the simulation results with the experimental results to validate the accuracy of the mathematical model. To consider the rheological properties, we calculate the specific viscosities of the PCM fluid. Additionally, we examine the effects of flow rate and PCM weight fraction on the melting mass and the recovered heat. We also calculate the relative circulation power of the loop and evaluate the net transportable energy and estimate the heat-storing time for the SCHP unit.

#### 3.1. Grid and Time-Step Independence

Meshing grid density and time step can affect the computational cost and accuracy of the simulation results. To verify the independence of grid density and time step on

the simulation results, this section verifies the independence of three different sizes of grids (the total elements number is  $9.5 \times 10^6$ ,  $1.5 \times 10^7$  and  $3.0 \times 10^7$ , respectively) and three different time steps (0.1 s, 1 s, and 5 s) on the simulation results. The mean absolute percentage errors (MAPEs) of temperature at four locations (Re inlet/outlet and SC inlet/outlet) were compared at different grid densities and time steps.

Table 4 presents the MAPEs results for grid independence. It considers the maximum elements number of  $3.0 \times 10^7$  as the actual value. The MAPEs of  $9.5 \times 10^6$  are 0.75~1.06% and that of  $1.5 \times 10^7$  are 0.33~0.35%. Considering the computational cost and memory usage, the grid density  $9.50 \times 10^6$  is adopted in this study. Table 5 displays the MAPEs results for time-step independence. It considers the minimum time step of 0.1 s as the actual value. This table shows that the time step only has minimal effect on the simulation results, and the MAPEs of 1 s and 5 s are distributed between 0.017% and 0.066%. Because of the computational cost and better convergence, the time step used in the sensible heat step is 1 s and when latent heat is involved it is 0.1 s.

**Table 4.** MAPEs for grid independence under 1 s.

| MAPE (%)          | $T_{re,in}$       |                   | $T_{re,out}$      |                   | $T_{sc,in}$       |                   | $T_{re,out}$      |                   |
|-------------------|-------------------|-------------------|-------------------|-------------------|-------------------|-------------------|-------------------|-------------------|
|                   | $9.5 \times 10^6$ | $1.5 \times 10^7$ |
| $3.0 \times 10^7$ | 0.86              | 0.34              | 0.75              | 0.34              | 0.98              | 0.35              | 1.06              | 0.33              |

**Table 5.** MAPEs for time-step independence under  $9.5 \times 10^6$  mesh density.

| MAPE (%) | $T_{re,in}$ |       | $T_{re,out}$ |       | $T_{sc,in}$ |       | $T_{re,out}$ |       |
|----------|-------------|-------|--------------|-------|-------------|-------|--------------|-------|
|          | 1 s         | 5 s   | 1 s          | 5 s   | 1 s         | 5 s   | 1 s          | 5 s   |
| 0.1 s    | 0.019       | 0.065 | 0.017        | 0.059 | 0.017       | 0.057 | 0.019        | 0.066 |

### 3.2. Verification of Simulation and Experimental Data

Figure 2 shows the recovered heat using pure silicone oil in simulations and experiments. The experimental data are introduced from the previous studies [44,45] and inducted in Figure 2. The aperture area of the solar collector used in the experiments is  $1 \text{ m}^2$ . The average solar irradiation from two experiments (1 L/min and 2 L/min) is  $1105 \text{ W/m}^2$  and  $1013 \text{ W/m}^2$ , respectively. After correcting for the effects of solar radiation on recovered heat, the recovered heat at different flow rates is 222 W at 1 L/min and 217 W at 2 L/min per  $1000 \text{ W/m}^2$  solar irradiation. Different flow rates have similar recovered heat under the same solar irradiation conditions.

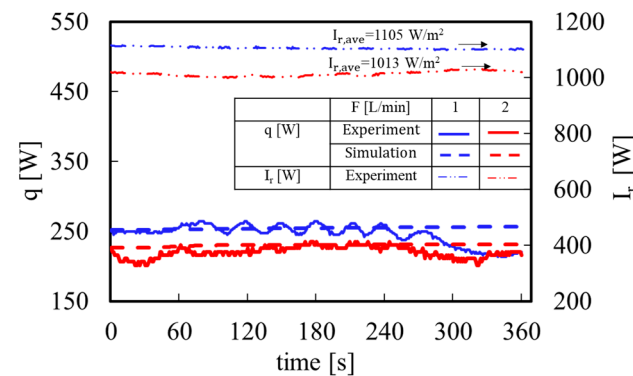


**Figure 2.** Recovered heat using pure silicone oil in simulations and experiments.

Meanwhile, using the same amount of solar irradiation, the simulated recovered heat is  $230 \text{ W/m}^2$  (1 L/min) and  $227 \text{ W/m}^2$  (2 L/min) per  $1000 \text{ W/m}^2$  solar irradiation. The absolute errors between the experiments and simulations are 3.6% at 1 L/min and 4.6%

at 2 L/min. The amount of recovered heat in the solar collector is used to determine the accuracy of the simulation model. The results shown in Figure 2 illustrate that the previously specified boundary conditions can be used.

### 3.3. Specific Viscosities of PCM Fluid

The flow behavior of the PCM fluid mixture varies greatly depending on the size, shape, distribution, mixing amount, etc. of the PCM particle. The Simha [46] equation is used to calculate the specific viscosity of the PCM fluid. The assumptions of the equation include the spherical monodisperse particles without agglomeration, as well as an ideal state in which only rigid body repulsion acts between particles. The Simha equation in Equation (19) shows that as the weight fraction by the PCM particles in the oil increases, the specific viscosity of the PCM fluid increases proportionally to the square of the volume fraction of the PCM particles.

$$\theta = 1 + 2.5 \left( \frac{\rho_{\text{oil}}}{\rho_{\text{PCM(s)}}} \omega \right) + 12.6 \left( \frac{\rho_{\text{oil}}}{\rho_{\text{PCM(s)}}} \omega \right)^2 \quad (19)$$

where  $\theta$  is the specific viscosity of the PCM fluid and  $\omega$  is the PCM weight fraction of the PCM fluid.

Figure 3 presents the specific viscosities of this PCM fluid on different PCM weight percentages. The specific viscosity is proportional to the square of the PCM weight fraction. At 20 wt% of PCM weight fraction, the specific viscosity is 1.53; at 10 wt%, the specific viscosity is 1.21. Therefore, to control the impact of the increase in specific viscosity on the pressure drop of the circulation, it is necessary to maintain the weight fraction of the PCM below 10 wt%.

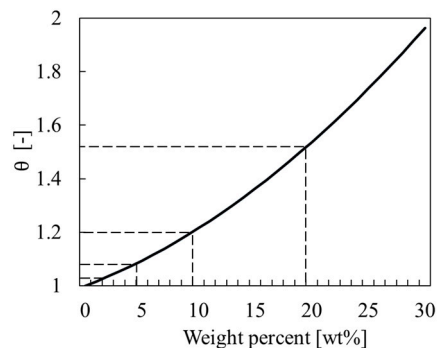


**Figure 3.** Effects of specific viscosities on different PCM weight percentages.

### 3.4. Effects of Flow Rates on Recovered Heat

In this subsection, four different flow rates of the PCM fluid are chosen to study the effects of flow rates on melting rate and enhanced recovered heat. The four flow rates in connecting pipes (CPs) are 0.5 L/min ( $8.3 \times 10^{-6} \text{ m}^3/\text{s}$ ), 1 L/min ( $1.6 \times 10^{-5} \text{ m}^3/\text{s}$ ), 2 L/min ( $3.3 \times 10^{-5} \text{ m}^3/\text{s}$ ), and 3 L/min ( $5 \times 10^{-5} \text{ m}^3/\text{s}$ ). The PCM fluid used in this subsection contains 10 wt% PCM, which was tested in previous studies [37]. The Reynolds numbers are 34, 67, 130, and 195, respectively (the physical properties of the mixture are calculated by volume average).

Figure 4a indicates the mass and melting percentage of liquid PCM over time at the SC outlet. As the PCM fluid is continuously circulated through the CPs between SC and Re, the melted PCM accumulates during the cycle. With the same content of PCM and in the first 30 min, 62% of the PCM is melted at the flow rate of 0.5 L/min, 30% is melted at 1 L/min, 14% is melted at 2 L/min, and 9% is melted at 3 L/min after liquid PCM is detected at the SC outlet. Melting mass increases as the flow rate decreases.

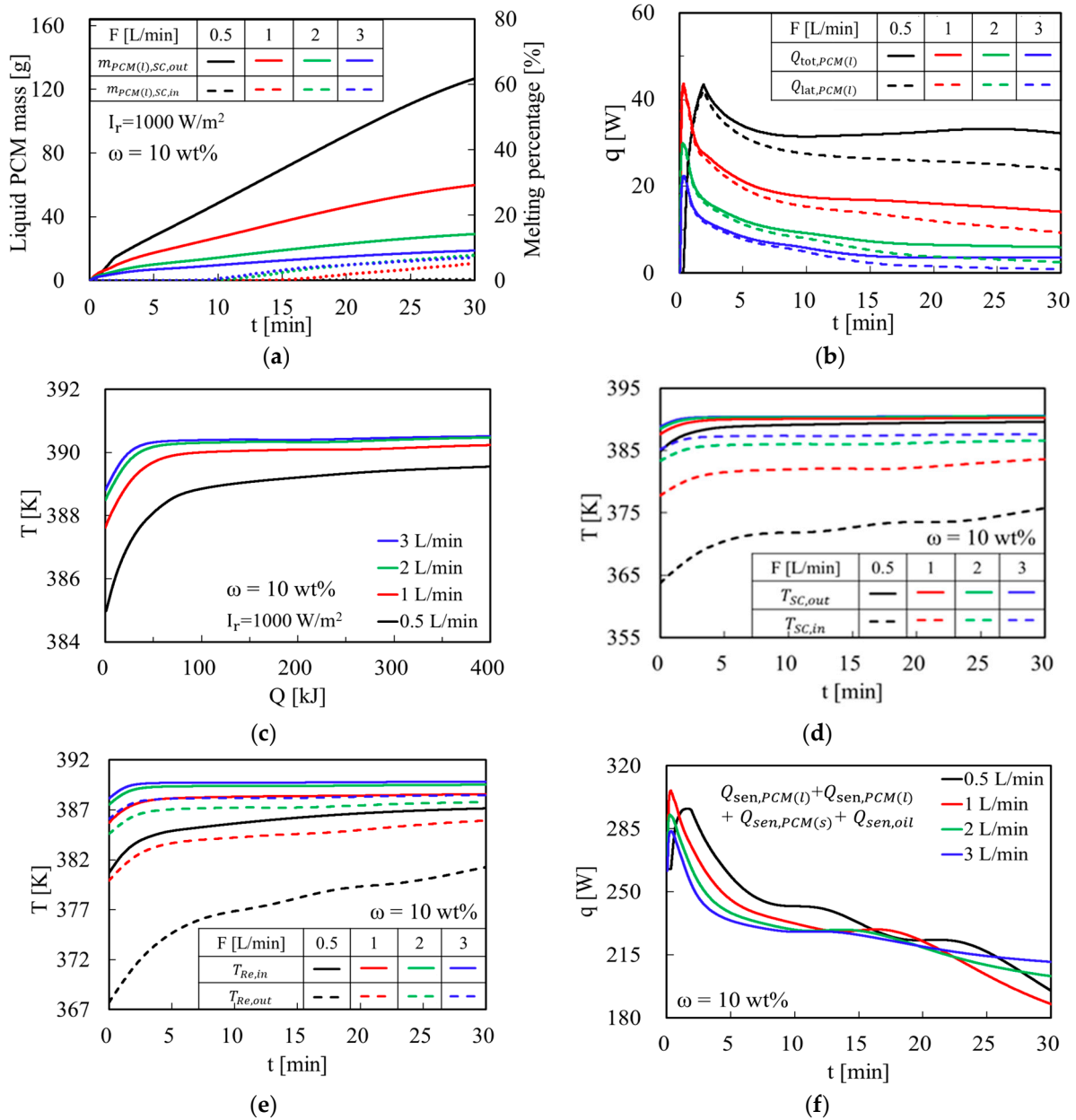


**Figure 4.** Several melting performances at different flow rates: (a) mass and melting percentage of liquid PCM over time at the SC outlet/inlet; (b) recovered heat forms liquid PCM; (c) total recovered heat (kJ) over temperature at the SC outlet; (d) temperature of PCM fluid at the SC inlet/outlet after melting over time; (e) temperature of PCM fluid at the Re inlet/outlet after melting over time; (f) Effects of flow rate on total recovered heat of PCM fluid, including sensible heat of silicone oil, solid PCM, liquid PCM, and latent heat of melting.

Figure 4b shows the recovered heat of liquid PCM. 1 L/min has the highest peak power, followed by 0.5 L/min, 2 L/min, and 3 L/min. The power from latent heat decreases significantly over time. In the cases of 1–3 L/min, as the flow rate decreases, the peak power gradually decreases. Due to the lower convective heat transfer in the case of 0.5 L/min, the peak-recovered heat appears later. Moreover, the average power is inversely proportional to the flow rate. This is because as the melting progresses, the PCM fluid with a lower flow rate can stay in the SC for a longer period of time. Hence under the conditions of the same solar heat flux, the PCM fluid with a lower flow rate receives more solar irradiance, and, therefore, the melting mass and recovered heat of the liquid PCM are significant.

Figure 4c presents the SC outlet temperature over total recovered heat (kJ). During the melting process, the difference in temperature change at the SC outlet among the three flow rates is small. In the melting temperature range, 2 L/min and 3 L/min are close, 1 L/min is lower, and 0.5 L/min is the lowest. This indicates that the PCM fluid at 0.5 L/min starts to melt earlier. Figure 4d,e display the temperature of PCM fluid at the SC and Re inlet/outlet after melting over time. The larger flow rate and PCM mass carries the greater latent heat. This results in a slower temperature rise at the inlet of the SC. Similarly, 0.5 L/min has the largest temperature rise at the Re outlet due to its lower heat capacity.

Figure 4f represents the total recovered heat of the PCM fluid (including sensible heat of silicone oil, solid PCM, liquid PCM, and latent heat). Compared to the recovered heat of pure silicone oil shown in Figure 2, the total recovered heat of 10 wt% PCM fluid in the SC is enhanced when the PCM starts melting. Compared to using pure silicone oil as HTF, the recovered heat at 0.5 L/min is enhanced to a maximum of 296 W and an average of 236 W, at 1 L/min is enhanced by a maximum of 1.33 times (from 230 W to 306 W) and an average of 1.01 times (from 230 W to 231 W), at 2 L/min is enhanced by a maximum of 1.29 times (from 227 W to 292 W) and an average of 1.01 times (from 227 W to 228 W), and at 3 L/min is enhanced by a maximum of 283 W and average of 227 W.

With the SC area of 1 m<sup>2</sup>, when solar irradiation is constant at 1000 W/m<sup>2</sup>, and after a continuous circulation of 30 min, Figure 5 presents the net transportation energy and circulation power of the loop under different flow rates at 30 min. At 30 min, the net transportation energy of PCM fluid from 0.5 L/min to 3 L/min is 415 kJ, 404 kJ, 393 kJ, and 383 kJ, respectively. Therefore, in these cases, the net transportation energy will increase as the flow rate decreases. In this case, lower flow rates (0.5 L/min and 1 L/min) can promote the recovered heat and net transportation energy.

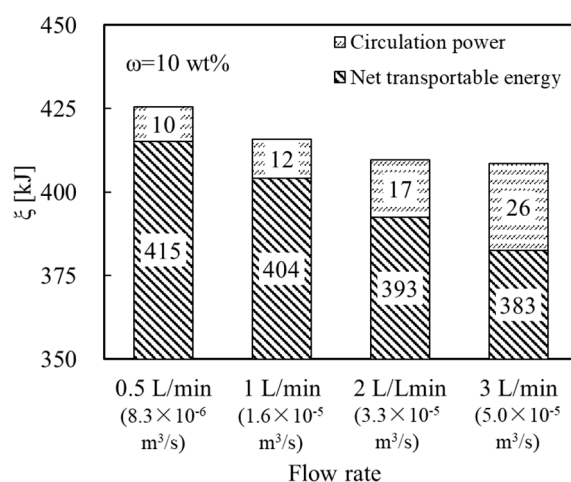
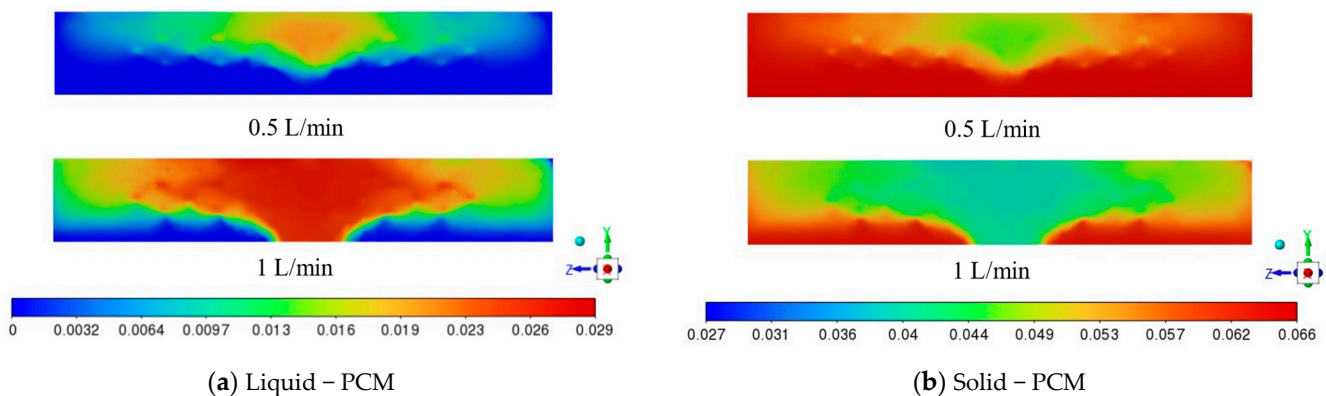


Figure 5. Effects of flow rates on net transportable energy and circulation power at 30 min.

However, Figure 6 presents the sectional view of 10 wt% PCM fluid at the Re inlet. The fraction of lower liquid PCM and higher solid PCM almost coincides. At 0.5 L/min, underdeveloped flow resulted in more solid PCM remaining at the bottom of the reactor, creating a “dead zone” and precipitation. In addition, underdeveloped flow caused by a low flow rate can lead to small heat transfer and mass transfer characteristics. For example, in the chemical heat-storing step, the fluid is used for heating the reactant, and the underdeveloped flow can reduce the heat transfer rate and cause hot spots on the reactant, leading to reduced efficiency and even equipment failure.



**Figure 6.** Sectional view (YZ – Plane,  $X = 0.039$  m) of 10 wt% PCM fluid at the Re inlet when the melted PCM is 80 g at the SC outlet.

Therefore, considering the above reasons, 1 L/min should be one of the best choices.

### 3.5. Effects of Weight Fractions of PCM on Recovered Heat

In this subsection, we investigated the effects of different PCM weight fractions on melting mass and recovered heat. The previous study [37] found that using 10 wt% PCM fluid in a straight pipe had little effect on pressure drop. However, due to the intricate piping in the SCHP unit, which includes the U-shaped pipes in the SC and heat exchange pipes of the Re, a higher particulate loading may lead to pipeline blockage and unstable flow path, resulting in greater pressure drop. To address this issue, we analyzed the performance of lower particulate loadings, specifically 2 wt% and 5 wt%.

Figure 7a displays the mass of liquid PCM at the SC inlet and outlet over time. When subjected to the same flow rates, a higher concentration of PCM results in a greater quantity of melted PCM within the same time interval, as predicted. However, the rate of increase in the amount of melted PCM decreases as the PCM concentration increases. Specifically, reducing the PCM content by 5 times (from 10 wt% to 2 wt%) does not correspondingly decrease the melting amount by the same factor. This phenomenon is likely due to Equation (15), which utilizes the temperature differential between the melting point and the PCM fluid temperature as the driving force for phase change. The increased specific heat of higher PCM concentrations inhibits the temperature growth, resulting in a lower melting mass. On the other hand, as Figure 7a,b show, the maximum amount of liquid PCM detected at the SC inlet is 2 wt% PCM fluid, likely due to the higher fluid temperature (Figure 7e,f) of the 2 wt% PCM fluid in the Re. This high temperature makes it more difficult for the PCM to solidify in the Re, allowing the liquid PCM to return directly to the SC without solidification.

Figure 7b presents the percentage of melting over time for different PCM contents. Within the first 30 min, only 29% of the PCM is melted using 10 wt%, 52% using 5 wt%, and 78% using 2 wt%. However, after 30 min, the melting speed of 2 wt% decreased to almost zero. Increasing the PCM contents can prolong the gain time of latent heat. Figure 5c illustrates the recovered heat of liquid PCM over time. The peak power of 10 wt%, 5 wt%, and 2 wt% PCM fluid is 44 W, 32 W, and 20 W, respectively. The average power of the three cases is 20 W, 17 W, and 11 W, respectively. Additionally, the latent power brought by 2 wt% is almost zero at 30 min, but there is still sensible heat power brought by the melted PCM.

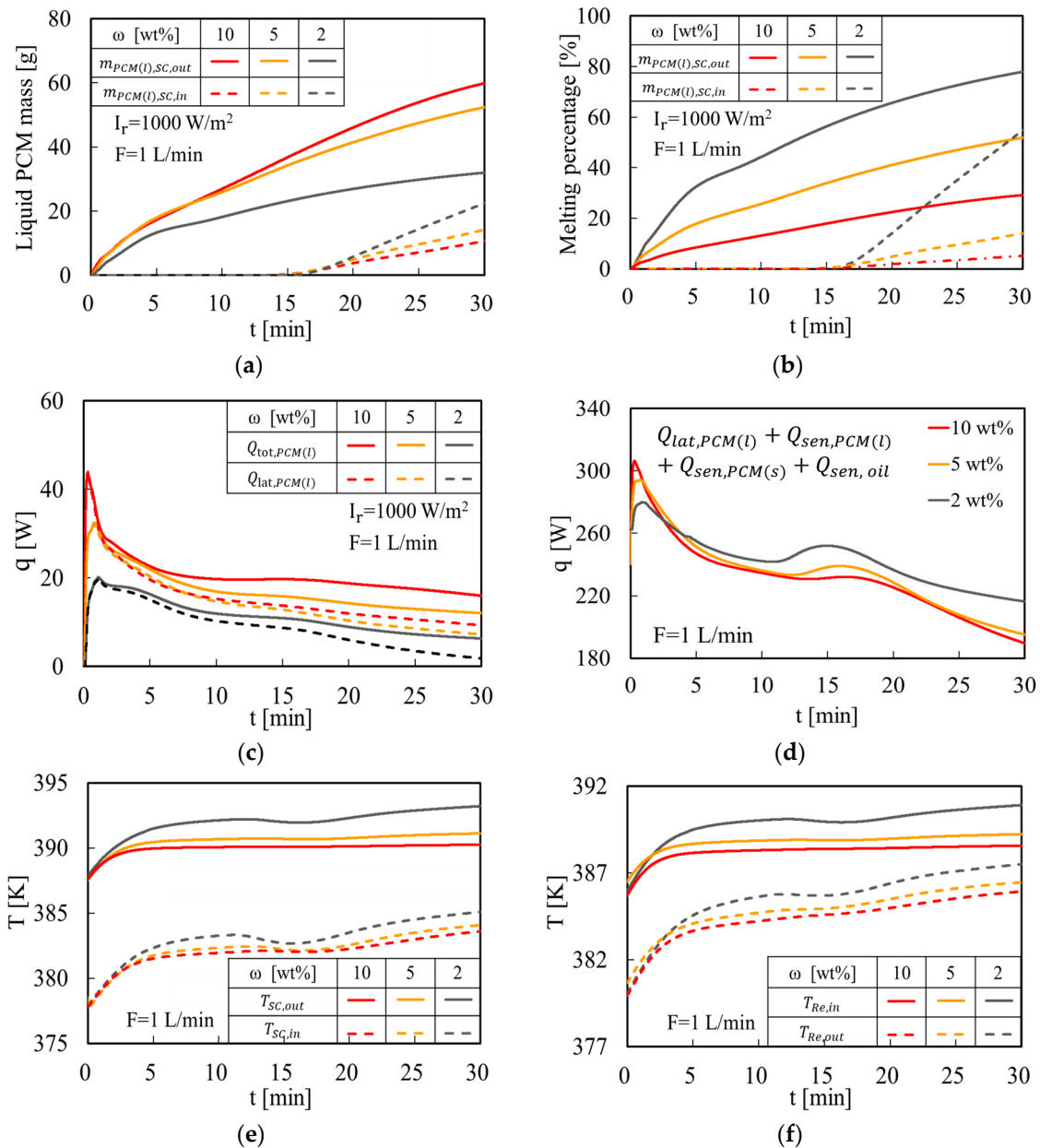


**Figure 7.** Several melting performances at different PCM weight fractions: (a) mass of liquid PCM over time; (b) melting percentage of liquid PCM over time; (c) recovered heat from liquid PCM; (d) effects of weight fraction on total recovered heat of PCM fluid, including sensible heat of silicone oil, solid PCM, and liquid PCM as well as latent heat; (e) temperature of PCM fluid at the SC inlet/outlet after melting over time; (f) temperature of PCM fluid at the Re inlet/outlet after melting over time.

Figure 7d demonstrates the effects of PCM weight fraction on the total recovered heat of PCM fluid. The temperature difference between the SC inlet and outlet directly affects the recovered heat of the SC. As shown in Figure 7e, the temperature difference for all three-weight fractions at the beginning of melting is 10 K, but after 30 min of melting, the minimum temperature difference of 10 wt% is 6.7 K, whereas the maximum temperature difference for 2 wt% is 8.1 K. This leads to a higher recovered heat of 2 wt% PCM. Compared to using pure silicone oil as HTF, the recovered heat using 10 wt% PCM is enhanced by a maximum of 1.33 times (from 230 W to 306 W) and an average of 1.01 times (from 230 W to 231 W), using 5 wt% is enhanced by a maximum of 1.28 times (from 230 W to 294 W) and an average of 1.02 times (from 230 W to 234 W), and using 2 wt% is enhanced by a

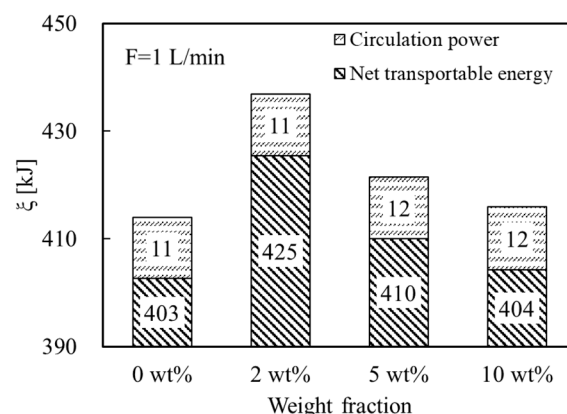
maximum of 1.22 times (from 230 W to 280 W) and an average of 1.06 times (from 230 W to 243 W).

Figure 7e,f respectively display the temperature of PCM fluid at the SC and Re inlet/outlet after melting over time. The three weight fractions exhibit varying degrees of temperature drop and rise. This phenomenon can be explained from a thermodynamic viewpoint. As the PCM absorbs heat during melting, it absorbs energy from its surroundings, including the heat from silicone oil, causing the temperature of the mixture to drop slightly. The heat absorbed by the PCM during melting reduces the total heat of the mixture. This temperature drop is relatively small and depends on factors such as the heating rate, the amount of PCM in the mixture, and the nature of the silicone oil.

When the PCM and silicone oil mixture is heated until the PCM melts, the smaller the amount of PCM in the mixture, the faster the temperature of the mixture will rise. As PCM melts, the heat capacity of the mixture decreases since liquid PCMs generally have a smaller heat capacity than solid PCMs. When the content of the PCM in the mixture is small, the total heat capacity of the mixture is small, and the same absorbed heat will lead to a larger temperature rise.

Therefore, using a 10 wt% PCM fluid will result in the smallest degree of temperature rise at the SC outlet due to its largest specific heat, while using a 2 wt% PCM fluid will result in the largest temperature rise due to its smallest specific heat. Moreover, the temperature rise of the fluids with different PCM contents is similar at the SC inlet since the difference in heat capacity between the three cases is small in the SC inlet. Combined with the above findings, the total recovered heat of 2 wt% PCM fluid is relatively large.

With the SC area of  $1 \text{ m}^2$ , when solar irradiation is constant at  $1000 \text{ W/m}^2$ , and after a continuous circulation of 30 min, Figure 8 presents the net transportation energy and circulation power of the loop under different flow rates at 30 min. At the flow rate of 1 L/min, compared to 0 wt% PCM fluid, when using 2 wt%, 5 wt%, and 10 wt% PCM fluid, the circulation power increases by 1.004, 1.012, and 1.028 times, respectively. At 30 min, the recovered heat of 0 wt%, 2 wt%, 5 wt%, and 10 wt% PCM fluid is 414 kJ, 436 kJ, 422 kJ, and 416 kJ, respectively, and the relative theoretical circulation power of the PCM fluids is 11.4 kJ, 11.4 kJ, 11.5 kJ, and 11.7 kJ, respectively. Therefore, in these cases, 2 wt% PCM fluid achieves the highest net transportable energy due to higher recovered heat and lower circulation power.



**Figure 8.** Effects of weight fractions on net transportable energy and circulation power at 30 min.

### 3.6. Estimation of Heat-Storing Time for SCHP Unit

In this subsection, we conduct a trial estimation of the shortening effect of using PCM fluid on the heat-storing time for the SCHP unit based on the above simulations. For example, 33% of the recovered heat will be used for the heat exchange of the reactor [8]. Meanwhile, it is assumed that the latent heat is completely released in the Re during the entire heat-storing step; furthermore, the condenser temperature is set at 288 K, the

equilibrium temperature of the reactant is 373 K, and the dehydration conversion of chemical heat storing can reach 100%.

The sensible heat-storing time and chemical heat-storing time of the reactant bed are calculated by the following formulas:

$$t_{\text{tot}} = t_{\text{sen}} + t_{\text{chem}} = \frac{Q_{\text{sen,p}} + Q_{\text{sen,re}} + Q_{\text{h}}}{60 \times Q_{\text{ex,re}}} = \frac{m_{\text{p}}c_{\text{p}}(T_{\text{p}} - T_{\text{atm}}) + m_{\text{re}}c_{\text{re}}(T_{\text{p}} - T_{\text{atm}}) + n_{\text{p}}\Delta H_{\text{p}}}{60 \times Q_{\text{ex,re}}} \quad (20)$$

The time of sensible heat storing is the sum of the sensible heat of the reactant bed  $Q_{\text{sen,p}}$  and the reactor  $Q_{\text{sen,re}}$  divided by the amount of heat exchange in the reactor  $Q_{\text{ex,re}}$ . The time of chemical heat storing is the chemical heat of the reactant  $Q_{\text{h}}$  divided by the amount of heat exchange in the reactor. Table 6 presents the amount of heat exchange in the reactor. Table 7 presents the demand energy in the reactor.

**Table 6.** Amount of heat exchange in the reactor.

| F                      | 1 L/min  |       |       |       |        |
|------------------------|----------|-------|-------|-------|--------|
|                        | $\omega$ | 0 wt% | 2 wt% | 5 wt% | 10 wt% |
| $Q_{\text{ex,re}}$ (W) |          | 75.9  | 80.2  | 77.2  | 76.2   |

**Table 7.** Demand energy in the reactor.

| $Q_{\text{sen,p}}$ (kJ) | $Q_{\text{sen,re}}$ (kJ) | $Q_{\text{h}}$ (kJ) |
|-------------------------|--------------------------|---------------------|
| 132                     | 223                      | 580                 |

The relationship between weight fraction and total heat-storing time is illustrated in Figure 9. For a fixed solar irradiation of 1000 W/m<sup>2</sup> and SC area of 1 m<sup>2</sup>, the pure silicone oil as the HTF requires a heat-storing time of 205 min. The shortest heat-storing time of 194 min is achieved using 2 wt% PCM fluid. As observed in this study, increasing the PCM content leads to an increase in the heat-storing time.

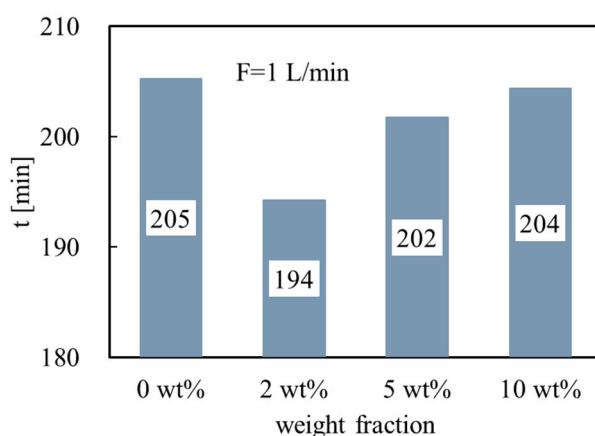


**Figure 9.** Effects of weight fraction on total heat-storing time.

#### 4. Conclusions

This study proposes a 3D dynamic simulation model to study the closed circulation of the heat transfer fluid (HTF) for the solar chemical heat pump (SCHP) unit. In this study, the HTF using the previously proposed PCM fluid is circulated in the solar collector (SC) to recover solar heat. The governing equations of the model are solved in ANSYS 2021 R2 consideration of the heat/mass transfer of phase changing in the PCM fluid. The following conclusions are found:

1. It is necessary to maintain the weight fraction of the PCM below 10 wt% to control the impact of the increase in specific viscosity on the circulation power of the circulation.
2. The melted mass and recovered heat of the PCM fluid are affected by flow rate, with a larger melted mass observed at lower flow rates due to longer residence time in the SC. A lower flow rate can enhance the PCM melted mass and the recovered heat although sensible heat amount increases with the flow rate. The best flow rate is 1 L/min when the SC area is 1 m<sup>2</sup>.
3. The higher PCM content has higher latent heat. On the other hand, the lower content PCM can increase the temperature difference between the SC inlet and outlet because of the lower PCM heat capacity.
4. The increase in the net transportable energy illustrates that using PCM fluid can increase the recovered heat without a significant increase in the circulation power. The maximum growth in this study is achieved with 2 wt% PCM fluid.
5. For the 1 L/min flow rate, 2 wt% PCM fluid has shorter heat-storing time and larger net transportable energy than 0 wt% PCM fluid (426 kJ←403 kJ) for the SCHP unit.

In summary, this study shows that the flow rate and weight fraction of PCM have significant impacts on the recovered heat and net transportable energy in the SC using PCM fluid. This study provides valuable insights into optimizing the design of SCs with PCM fluid to enhance their thermal performance. These results are important for the design and optimization of solar thermal systems such as SCHP using PCM fluids.

**Author Contributions:** Conceptualization, H.O.; formal analysis, Y.R.; writing—original draft preparation, Y.R.; writing—review and editing, H.O.; supervision, H.O. All authors have read and agreed to the published version of the manuscript.

**Funding:** This research was funded by JSPS KAKENHI Grant Number 20K04302.

**Data Availability Statement:** Data sharing is not applicable to this article.

**Acknowledgments:** This work was supported by JSPS KAKENHI Grant Number 20K04302.

**Conflicts of Interest:** The authors declare no conflict of interest.

## Nomenclature

|            |                                |                       |
|------------|--------------------------------|-----------------------|
| $T$        | Temperature                    | (K)                   |
| $q$        | Heat                           | (W)                   |
| $P$        | Pressure                       | (kPa)                 |
| $\lambda$  | Effective thermal conductivity | (W/mK)                |
| $\eta$     | Reflectance                    | (-)                   |
| $\tau$     | Transmittance                  | (-)                   |
| $\sigma$   | Absorbance                     | (-)                   |
| $h$        | Heat transfer coefficient      | (W/m <sup>2</sup> K)  |
| $I$        | Irradiation                    | (W/m <sup>2</sup> )   |
| $\dot{m}$  | Mass transfer rate             | (kg/m <sup>3</sup> s) |
| $\Delta H$ | Enthalpy                       | (J/kg)                |
| $\omega$   | Weight fraction                | (wt%)                 |
| $Q$        | Recovered heat                 | (W)                   |
| $\xi$      | Net transportable energy       | (kJ)                  |
| $W$        | Circulation power              | (kJ)                  |
| $F$        | Flow rate                      | (L/min)               |
| $S$        | Volumetric heat source         | (W/m <sup>3</sup> )   |
| $\rho$     | Mixture density                | (kg/m <sup>3</sup> )  |
| $Z$        | Body force                     | (N/m <sup>3</sup> )   |
| $\mu$      | Viscosity of multiphase flow   | (Pas)                 |

|            |                                     |        |
|------------|-------------------------------------|--------|
| $\Delta P$ | Pressure drop                       | (kPa)  |
| $t$        | Time                                | (min)  |
| $v$        | Velocity                            | (m/s)  |
| $M$        | Energy loss in the circulation      | (J/kg) |
| $\alpha$   | Volume fraction                     | (-)    |
| $\theta$   | Specific viscosity                  | (-)    |
| Subscripts |                                     |        |
| atm        | Atmosphere                          |        |
| g          | Glass                               |        |
| r          | Solar irradiation                   |        |
| th         | Pipes in reactor                    |        |
| f          | Frame of reactor                    |        |
| m          | Melting point                       |        |
| l          | Liquid phase                        |        |
| s          | Solid phase                         |        |
| pump       | Circulation pump                    |        |
| loss       | Energy loss                         |        |
| fr         | Piping friction                     |        |
| lat        | Latent heat                         |        |
| lo         | Local elements                      |        |
| int        | Internal                            |        |
| in         | Input                               |        |
| c          | Circulation                         |        |
| sen        | Sensible heat storing               |        |
| chem       | Chemical heat storing               |        |
| p          | Particle in reactant bed            |        |
| h          | Hot heat from chemical heat storing |        |
| ex         | Exchange heat                       |        |
| tot        | Total                               |        |

## References

1. Ministry of Foreign Affairs of Japan Prime Minister Suga's Attendance at the Leaders Summit on Climate. Available online: [https://www.mofa.go.jp/ic/ch/page6e\\_000236.html](https://www.mofa.go.jp/ic/ch/page6e_000236.html) (accessed on 28 September 2022).
2. Ogura, H.; Miyazaki, M.; Matsuda, H.; Hasatani, M.; Yanadori, M.; Hiramatsu, M. Numerical Analysis of Heat Transfer in Particle-Bed Reactor with Fins in Chemical Heat Pump Using Ca(OH)<sub>2</sub>/CaO Reaction. *Kagaku Kogaku Ronbunshu* **1992**, *18*, 669–676. (In Japanese) [[CrossRef](#)]
3. Ogura, H.; Yamamoto, T.; Kage, H. Efficiencies of CaO/H<sub>2</sub>O/Ca(OH)<sub>2</sub> Chemical Heat Pump for Heat Storing and Heating/Cooling. *Energy* **2003**, *28*, 1479–1493. [[CrossRef](#)]
4. Ogura, H.; Yasuda, S.; Otsubo, Y.; Mujumdar, A.S. Continuous Operation of a Chemical Heat Pump. *Asia-Pac. J. Chem. Eng.* **2007**, *2*, 118–123. [[CrossRef](#)]
5. Oguraa, H. Energy Recycling System Using Chemical Heat Pump Container. *Energy Procedia* **2012**, *14*, 2048–2053. [[CrossRef](#)]
6. Ogura, H.; Mikami, H.; Suzuki, H. Enhancement of Refrigeration Cold-Heat Production by Thermal Driven Chemical Heat Pump. *Trans. JSRAE* **2015**, *32*, 373–379. [[CrossRef](#)]
7. Lai, L.; Imai, T.; Umezu, M.; Ishii, M.; Ogura, H. Possibility of Calcium Oxide from Natural Limestone Including Impurities for Chemical Heat Pump. *Energies* **2020**, *13*, 803. [[CrossRef](#)]
8. Ren, Y.; Ogura, H. Performance Evaluation of Off-Grid Solar Chemical Heat Pump for Cooling/Heating. *Sol. Energy* **2021**, *224*, 1247–1259. [[CrossRef](#)]
9. Liu, W.; Bie, Y.; Xu, T.; Cichon, A.; Królczyk, G.; Li, Z. Heat Transfer Enhancement of Latent Heat Thermal Energy Storage in Solar Heating System: A State-of-the-Art Review. *J. Energy Storage* **2022**, *46*, 103727. [[CrossRef](#)]
10. Ling, Z.; Wen, X.; Zhang, Z.; Fang, X.; Gao, X. Thermal Management Performance of Phase Change Materials with Different Thermal Conductivities for Li-Ion Battery Packs Operated at Low Temperatures. *Energy* **2018**, *144*, 977–983. [[CrossRef](#)]
11. Zauner, C.; Hengstberger, F.; Etzel, M.; Lager, D.; Hofmann, R.; Walter, H. Experimental Characterization and Simulation of a Fin-Tube Latent Heat Storage Using High Density Polyethylene as PCM. *Appl. Energy* **2016**, *179*, 237–246. [[CrossRef](#)]
12. Deng, S.; Nie, C.; Jiang, H.; Ye, W.B. Evaluation and Optimization of Thermal Performance for a Finned Double Tube Latent Heat Thermal Energy Storage. *Int. J. Heat Mass Transf.* **2019**, *130*, 532–544. [[CrossRef](#)]

13. Nguyen, T.P.; Ramadan, Z.; Hong, S.J.; Park, C.W. Effect of Graphite Fin on Heat Transfer Enhancement of Rectangular Shell and Tube Latent Heat Storage. *Int. J. Heat Mass Transf.* **2022**, *194*, 123018. [[CrossRef](#)]
14. Choi, J.C.; Kim, S.D. Heat Transfer in a Latent Heat-Storage System Using MgCl<sub>2</sub>·6H<sub>2</sub>O at the Melting Point. *Energy* **1995**, *20*, 13–25. [[CrossRef](#)]
15. Liu, X.; Huang, Y.; Zhang, X.; Zhang, C.; Zhou, B. Investigation on Charging Enhancement of a Latent Thermal Energy Storage Device with Uneven Tree-like Fins. *Appl. Therm. Eng.* **2020**, *179*, 115749. [[CrossRef](#)]
16. Dekhil, M.A.; Simo Tala, J.V.; Bulliard-Sauret, O.; Bougeard, D. Numerical Analysis of the Performance Enhancement of a Latent Heat Storage Shell and Tube Unit Using Finned Tubes during Melting and Solidification. *Appl. Therm. Eng.* **2021**, *192*, 116866. [[CrossRef](#)]
17. Tang, S.; Zhou, J.; Shen, C.; Zhang, D. Thermal Performance Analysis and Optimization of Melting Process in a Buried Tube Latent Heat Storage System. *J. Energy Storage* **2022**, *52*, 104863. [[CrossRef](#)]
18. Ermis, K.; Ereğ, A.; Dincer, I. Heat Transfer Analysis of Phase Change Process in a Finned-Tube Thermal Energy Storage System Using Artificial Neural Network. *Int. J. Heat Mass Transf.* **2007**, *50*, 3163–3175. [[CrossRef](#)]
19. Tay, N.H.S.; Belusko, M.; Bruno, F. Designing a PCM Storage System Using the Effectiveness-Number of Transfer Units Method in Low Energy Cooling of Buildings. *Energy Build.* **2012**, *50*, 234–242. [[CrossRef](#)]
20. Elbahjaoui, R.; El Qarnia, H. Thermal Analysis of Nanoparticle-Enhanced Phase Change Material Solidification in a Rectangular Latent Heat Storage Unit Including Natural Convection. *Energy Build.* **2017**, *153*, 1–17. [[CrossRef](#)]
21. Motahar, S.; Alemrajabi, A.A.; Khodabandeh, R. Experimental Study on Solidification Process of a Phase Change Material Containing TiO<sub>2</sub> Nanoparticles for Thermal Energy Storage. *Energy Convers. Manag.* **2017**, *138*, 162–170. [[CrossRef](#)]
22. Gunjo, D.G.; Jena, S.R.; Mahanta, P.; Robi, P.S. Melting Enhancement of a Latent Heat Storage with Dispersed Cu, CuO and Al<sub>2</sub>O<sub>3</sub> Nanoparticles for Solar Thermal Application. *Renew. Energy* **2018**, *121*, 652–665. [[CrossRef](#)]
23. Hwang, Y.; Lee, J.K.; Lee, C.H.; Jung, Y.M.; Cheong, S.I.; Lee, C.G.; Ku, B.C.; Jang, S.P. Stability and Thermal Conductivity Characteristics of Nanofluids. *Thermochim. Acta* **2007**, *455*, 70–74. [[CrossRef](#)]
24. Xie, H.; Lee, H.; Youn, W.; Choi, M. Nanofluids Containing Multiwalled Carbon Nanotubes and Their Enhanced Thermal Conductivities. *J. Appl. Phys.* **2003**, *94*, 4967–4971. [[CrossRef](#)]
25. Baobao, Z.; Nan, Z. Nano Express Open Acceptation of Stable Magnetic Nanofluids Containing Fe<sub>3</sub>O<sub>4</sub>@ppy Nanoparticles by a Novel One-Pot Route. *Nanoscale Res. Lett.* **2011**, *6*, 230. [[CrossRef](#)]
26. Xie, H.; Wang, J.; Xi, T.; Liu, Y.; Ai, F.; Wu, Q. Thermal Conductivity Enhancement of Suspensions Containing Nanosized Alumina Particles. *J. Appl. Phys.* **2002**, *91*, 4568–4572. [[CrossRef](#)]
27. Xuan, Y.; Li, Q. Heat Transfer Enhancement of Nanofluids. *Int. J. Heat Fluid Flow* **2000**, *21*, 58–64. [[CrossRef](#)]
28. Abandani, M.H.S.; Ganji, D.D. Melting Effect in Triplex-Tube Thermal Energy Storage System Using Multiple PCMs-Porous Metal Foam Combination. *J. Energy Storage* **2021**, *43*, 103154. [[CrossRef](#)]
29. Nedjem, K.; Teggat, M.; Hadibi, T.; Arıcı, M.; Yıldız, Ç.; Ismail, K.A.R. Hybrid Thermal Performance Enhancement of Shell and Tube Latent Heat Thermal Energy Storage Using Nano-Additives and Metal Foam. *J. Energy Storage* **2021**, *44*, 103347. [[CrossRef](#)]
30. Hashem Zadeh, S.M.; Ghodrati, M.; Ayoubi Ayoubloo, K.; Sedaghatizadeh, N.; Taylor, R.A. Partial Charging/Discharging of Bio-Based Latent Heat Energy Storage Enhanced with Metal Foam Sheets. *Int. Commun. Heat Mass Transf.* **2022**, *130*, 105757. [[CrossRef](#)]
31. NematpourKesheteli, A.; Iasiello, M.; Langella, G.; Bianco, N. Enhancing PCMs Thermal Conductivity: A Comparison among Porous Metal Foams, Nanoparticles and Finned Surfaces in Triplex Tube Heat Exchangers. *Appl. Therm. Eng.* **2022**, *212*, 118623. [[CrossRef](#)]
32. Kaizawa, A.; Kamano, H.; Kawai, A.; Jozuka, T.; Senda, T.; Maruoka, N.; Akiyama, T. Thermal and Flow Behaviors in Heat Transportation Container Using Phase Change Material. *Energy Convers. Manag.* **2008**, *49*, 698–706. [[CrossRef](#)]
33. Kunkel, S.; Teumer, T.; Dörnhöfer, P.; Schlachter, K.; Weldeleslasie, Y.; Kühr, M.; Rädle, M.; Repke, J.U. Determination of Heat Transfer Coefficients in Direct Contact Latent Heat Storage Systems. *Appl. Therm. Eng.* **2018**, *145*, 71–79. [[CrossRef](#)]
34. Nomura, T.; Tsubota, M.; Sagara, A.; Okinaka, N.; Akiyama, T. Performance Analysis of Heat Storage of Direct-Contact Heat Exchanger with Phase-Change Material. *Appl. Therm. Eng.* **2013**, *58*, 108–113. [[CrossRef](#)]
35. Nomura, T.; Tsubota, M.; Oya, T.; Okinaka, N.; Akiyama, T. Heat Release Performance of Direct-Contact Heat Exchanger with Erythritol as Phase Change Material. *Appl. Therm. Eng.* **2013**, *61*, 28–35. [[CrossRef](#)]
36. Guo, S.; Zhao, J.; Wang, W.; Jin, G.; Wang, X.; An, Q.; Gao, W. Experimental Study on Solving the Blocking for the Direct Contact Mobilized Thermal Energy Storage Container. *Appl. Therm. Eng.* **2015**, *78*, 556–564. [[CrossRef](#)]
37. Hirose, Y.; Watanabe, K.; Hirano, Y.; Ogura, H. Studies on Flow of Latent/Sensible Heat Exchange Medium Composed of Erythritol and Silicone Oil for Improvement of Heat Transportation Efficiency. *Kagaku Kogaku Ronbunshu* **2023**. Submitted (In Japanese)
38. Ren, Y.; Ogura, H. Numerical Investigation on Performance Improvement of CaSO<sub>4</sub> Solar Chemical Heat Pump. *J. Therm. Sci. Technol.* **2022**, *17*, 22–58. [[CrossRef](#)]
39. Kobayashi, E.; Hirose, Y.; Ogura, H. Improvement of Evaporator Performance in Chemical Refrigerator—Effects of Aqueous Solution Components and Mass Transfer. *Trans. Jpn. Soc. Refrig. Air Cond. Eng.* **2020**, *37*, 233–240. (In Japanese)
40. ANSYS, Inc. *ANSYS Fluent Theory Guide, Release 2021 R1*; ANSYS, Inc.: Canonsburg, PA, USA, 2021.

41. Wang, W.; He, S.; Guo, S.; Yan, J.; Ding, J. A Combined Experimental and Simulation Study on Charging Process of Erythritol–HTO Direct-Blending Based Energy Storage System. *Energy Convers. Manag.* **2014**, *83*, 306–313. [[CrossRef](#)]
42. Brackbill, J.U.; Kothe, D.B.; Zemach, C. A Continuum Method for Modeling Surface Tension. *J. Comput. Phys.* **1992**, *100*, 335–354. [[CrossRef](#)]
43. Lee, W.H. A Pressure Iteration Scheme for Two-Phase Modeling. Technical Report LA-UR 79-975. 1979. Available online: [https://www.worldscientific.com/doi/10.1142/9789814460286\\_0004](https://www.worldscientific.com/doi/10.1142/9789814460286_0004) (accessed on 15 March 2023).
44. Ri, H.; Hirose, Y.; Ogura, H. Studies on Latent Heat Transportation Medium for Solar Heat Collection at 373–423 K. In Proceedings of the Japanese Society for Multiphase Flow 2022 Symposium, SS-C E0062, Online, 19 August 2022.
45. Ren, Y.; Ri, H.; Hirose, Y.; Ogura, H. Numerical Studies on Heat/Mass Transfer Enhancement of PCM Fluid for Solar Chemical Heat Pump. In Proceedings of the Grand Renewable Energy 2022 International Conference (GRE2022), Online, 13–20 December 2022.
46. Simha, R. A Treatment of the Viscosity of Concentrated Suspensions. *J. Appl. Phys.* **1952**, *23*, 1020–1024. [[CrossRef](#)]

**Disclaimer/Publisher’s Note:** The statements, opinions and data contained in all publications are solely those of the individual author(s) and contributor(s) and not of MDPI and/or the editor(s). MDPI and/or the editor(s) disclaim responsibility for any injury to people or property resulting from any ideas, methods, instructions or products referred to in the content.